Energy Gain Kernel for Climate Feedbacks. Part II: Spatial Pattern of Surface Amplification Factor and Its Dependency on Climate Mean State

XIAOMING HU,[a,b] MING CAI,[c] JIE SUN,[c] FENG DING,[d] AND JING FENG[e]

[a] *School of Atmospheric Sciences, Sun Yat-sen University and Southern Marine Science and Engineering Guangdong Laboratory, Zhuhai, China*
[b] *Guangdong Province Key Laboratory for Climate Change and Natural Disaster Studies, Zhuhai, China*
[c] *Department of Earth, Ocean, and Atmospheric Science, Florida State University, Tallahassee, Florida*
[d] *Department of Atmospheric and Oceanic Sciences, Peking University, Beijing, China*
[e] *Atmospheric and Oceanic Sciences Program, Princeton University, Princeton, New Jersey*

(Manuscript received 30 April 2024, in final form 10 October 2024, accepted 19 December 2024)

ABSTRACT: In this study, we examine the spatial pattern of the surface amplification factor (SAF). SAF corresponds to the surface element of the energy gain kernel derived in Part I of this three-part series papers, representing the amplification rate of input energy perturbations at the surface. At a given location, SAF amplifies surface energy perturbations at an equal rate regardless of their origins. Therefore, the spatial variation of SAF can provide insight into the spatial variability of climate sensitivity. The global mean of SAF is about 2.6, and its spatial pattern closely resembles the climate mean cloud field. SAF values range from 4 over the western equatorial Pacific, 2.8–3.2 over midlatitude storm-track regions, and 2.0–2.8 over the Arctic, to 1.4–1.7 over the Antarctic. The more longwave (LW) absorbers in the atmosphere, the greater SAF. Therefore, SAF is greater in regions where atmospheric water vapor is abundant such as the tropics, and where clouds are prevalent such as midlatitude storm tracks and the Arctic, but it is smaller and close to unity in cold, high-elevated regions. Moreover, SAF tends to negatively correlate with surface temperature when LW absorbers are abundant and positively when they are scarce. With limited LW absorbers, SAF exhibits a negative (positive) correlation in cold (warm) conditions. While the spatial pattern of surface temperature plays a secondary role in shaping SAF, it may help explain why the climate sensitivity in models can either increase or decrease with surface temperature depending on the LW absorbers in the atmosphere.

KEYWORDS: Climate sensitivity; Longwave radiation; Radiative transfer; Absorption; Feedback

1. Introduction

The climate state dependence of equilibrium climate sensitivity (ECS) and climate feedback processes has received a great attention recently (Colman and McAvaney 2009; Caballero and Huber 2013; Forster et al. 2021). The most widely embraced concept is that ECS or the total climate feedback parameter tends to increase with rising climate mean global temperature (Randall et al. 2018; Mauritsen et al. 2019; Anagnostou et al. 2020). Such positive temperature dependence is evident in both paleoclimate records (Caballero and Huber 2013; von der Heydt and Ashwin 2016; Zhu et al. 2019) and climate model simulations (Hansen et al. 2013; Bloch-Johnson et al. 2021). Additionally, the instantaneous radiative forcing due to increased CO_2 concentrations also depends on the climatological mean state, potentially leading to a higher ECS when accounting for state dependence of the climate feedback strength (He et al. 2023). However, evidence suggests that this positive temperature dependence may not equally exist across different climate models (Martínez-Botí et al. 2015; Stolpe et al. 2019). Stolpe et al. (2019) found that the global mean warming simulated by CESM1 is independent of the initial climate state, although the local climate responses, such as high-latitude warming, may strongly depend on the mean state due to the surface albedo feedback. Furthermore, there is a lack of evidence for stronger feedback strength in the warm Pliocene than the cooler Pleistocene (Martínez-Botí et al. 2015). In terms of the intermodel spread in CMIP5, there is a negative correlation between the climate sensitivity and climate mean global temperature (Hu et al. 2017b).

Many studies have investigated the underlying physical mechanisms for the state dependence of individual feedback processes (Meraner et al. 2013). The positive temperature dependence has been attributed to the combined effect of water vapor and cloud feedbacks (Yoshimori et al. 2011; Caballero and Huber 2013; Meraner et al. 2013; Andrews and Webb 2018; Zhu et al. 2019; Bjordal et al. 2020; Rugenstein et al. 2020). The increase in water vapor feedback strength with rising climate mean temperature is due to the narrowing of the atmospheric window for the outgoing longwave radiation (OLR). The cloud feedback operates differently depending on the climate mean state, and its state dependence is more complex (Senior and Mitchell 2000; Andrews and Webb 2018; Bjordal et al. 2020). In warmer climates, cloud ice water content decreases while cloud liquid water increases (Bjordal et al. 2020). Due to their larger particle sizes, ice clouds are generally less opaque and less reflective than liquid clouds. Consequently, a warmer climate with less ice clouds but more liquid clouds tends to have a stronger positive cloud feedback, resulting in greater climate sensitivity (Yoshimori et al. 2011;

Denotes content that is immediately available upon publication as open access.

Corresponding author: Ming Cai, mcai@fsu.edu

DOI: 10.1175/JAS-D-24-0079.1

Pierrehumbert 2013; Zhu and Poulsen 2020). However, ice albedo and lapse-rate feedbacks are negatively correlated with climate mean temperature. Specifically, the ice albedo feedback is stronger in colder climates, favoring stronger warming under the same climate forcing in models with colder mean temperature and more ice coverage (Hu et al. 2017b). The strength of surface albedo feedback decreases continually as the climate warms due to diminishing snow and sea ice coverage (Senior and Mitchell 2000). Additionally, lapse-rate feedback acts to dampen climate sensitivity as climate mean temperature increases (Po-Chedley et al. 2018; Boeke et al. 2021). In general, the lapse-rate feedback is positive in the ice-covered regions but negative in the tropics (Boeke et al. 2021; Colman and Soden 2021; Sejas et al. 2021; Beer and Eisenman 2022). Whether the lapse-rate feedback is positive or negative depends on the dominant type of underlying surface. During the Last Glacial Maximum (LGM) period, in which Earth's surface is mainly covered by ice, the positive lapse-rate feedback over ice-coved regions outweighs the negative lapse-rate feedback over non-ice-covered regions (Yoshimori et al. 2009, 2011; Yoshimori and Suzuki 2019). During the current warm period, the ice-covered surface is limited to high mountains and high latitudes, resulting in the dominance of negative feedback nature of the lapse-rate feedback.

Hu et al. (2017b) also found that models with a warmer climate state generally exhibit a stronger water vapor feedback, leading to more substantial global warming under the same anthropogenic radiative forcing. The varying dependency of climate sensitivity on climate mean temperature—showing a negative correlation through ice albedo feedback and a positive correlation though water vapor feedback—contributes to the generally weaker correlation between intermodel spreads of global warming projections and climate mean temperature (Hu et al. 2017b). Hu et al. (2020) identified two dominant spatial patterns of uncertainties in projected surface warming. One pattern is for uncertainties in polar regions, driven mainly by the spread in ice albedo feedback. The other pattern is for uncertainties elsewhere, resulting from the intermodel spread of water vapor feedback. These two feedback processes account for 71.3% of the intermodel spread in the spatial warming pattern and 98.7% of the spread in global mean warming projections under the CMIP5 RCP8.5 scenario.

Recent studies of Cai et al. (2023) and Sun et al. (2024) examine factors affecting the slope of the quasi-linear relation between OLR and surface temperature based on latitudinal variations. These studies provide insights on the varying dependency of climate sensitivity on climate mean temperature.[1] Specifically, processes that enhance the meridional temperature gradient without affecting the meridional gradient of OLR lead to a gentler slope in the quasi-linear relation, implying stronger climate sensitivity. Atmospheric poleward energy transport reduces the latitudinal gradient of OLR more than the meridional gradient of surface temperature. This further decreases the quasi-linear slope of the OLR and surface temperature relation. It follows that climate models with warmer mean temperatures would exhibit a stronger meridional gradient in water vapor and enhanced poleward energy transport (e.g., Lu and Cai 2010; Hu et al. 2017a). Consequently, the quasi-linear slope of the OLR and surface temperature relation becomes gentler in a warmer world. This corresponds to a positive correlation between climate sensitivity and climate mean temperature. Because of the dependency of the ice albedo feedback strength on climate mean ice coverage, climate models with colder global mean temperature but the same meridional temperature gradient would also exhibit a higher climate sensitivity. This scenario corresponds to a negative correlation between climate sensitivity and climate mean temperature.

The overarching goal of the three-series papers is to establish a theoretical framework that effectively and objectively isolates the climate mean state information from feedback information for studies on climate sensitivity and feedback. In Cai et al. (2024, hereafter referred to as Part I), we formulated a new climate feedback kernel, referred to as the "energy gain kernel" (EGK), based on radiative transfer principles. The EGK amplifies input energy perturbations, whether due to external forcing or internal responses of nontemperature feedback to external forcing. The resultant energy perturbations are the total energy perturbations amplified through radiative thermal coupling within an atmosphere–surface column. Larger values of EGK indicate a greater ability to amplify the initial energy perturbation and vice versa.

The EGK is equal to the product of the diagonal matrix of the Planck feedback matrix and the inverse of the full Planck feedback matrix. The Planck feedback matrix can be obtained from climate mean states using a radiative transfer model by perturbing temperature fields at individual layers (Cai and Lu 2009; Lu and Cai 2009). Thus, there is an inherent connection between EGK and climate mean states. The diagonal elements of the Planck feedback matrix are proportional to the cubic power of climate mean temperatures of individual layers. They measure the thermal emission ability of individual atmospheric layers per unit warming. The strength of the EGK, on the other hand, is mainly determined by the amount of infrared absorbers in the climate mean atmosphere. Applying the EGK to the energy perturbations due to external forcing and individual nontemperature feedback processes, and then summing them up, yields the total amplified input energy perturbations. The ratio of the amplified input energy perturbation to the emission rate perturbations per 1-K warming of individual layers (i.e., the diagonal elements of the Planck feedback matrix) corresponds to the total temperature change in response to the external energy perturbation. This demonstrates the new feedback analysis framework's capability to explicitly separate the climate mean state from feedback processes. This

[1] We note here that the slope of the quasi-linear OLR–surface temperature relation derived from their spatial variation is not equal to its counterpart in the definition of the climate sensitivity parameter, which is typically estimated as the slope of the OLR–surface temperature from their temporal variations. Recent studies of Zhang et al. (2020) and McKim et al. (2021) found that the spatial mean of the slope of the OLR–surface temperature relation derived from their temporal variations is equivalent to its counterpart derived from their spatial variations.

separation provides insights into the origins of the intermodel spread of global warming projections.

In Part II, our focus centers on examining the spatial pattern of the surface element of EGK, referred to as surface amplification factor (SAF). We calculate the EGK using a radiative transfer model with input fields from the climate mean state of reanalysis dataset. We will discuss how the spatial pattern of SAF is shaped by variables affecting the climate mean infrared opacity, namely, water vapor, clouds, and surface pressure. Our discussion focuses on the spatial patterns of vertically integrated longwave (LW) absorbers (i.e., water vapor and clouds), although their vertical profiles also influence the spatial pattern of SAF. The dependence of SAF on T_S is complex because it is jointly determined by thermal emission spectrum and absorption spectrum, both of which are sensitive to temperature. For simplicity, our focus is on the observational and theoretical evidence for the intricate link between SAF and surface temperature T_S, although air temperatures following different lapse rates also influence the strength and spatial pattern of SAF.

The organization of Part II is as follows. Section 2 describes the data used in this study. Section 3 discusses the physical meaning of SAF. Section 4 is devoted to the influence of the amount of LW absorbers in the atmosphere on the strength of SAF, focusing on how the spatial patterns of water vapor, clouds, and surface pressure shape the spatial pattern of SAF. Section 5 examines the presence of positive and/or negative correlations between SAF and T_S, depending on the abundance level of LW absorbers in the atmosphere. Section 6 summarizes the main findings of this paper and discusses their key implications.

2. Data

The data used in Part II are the same as in Part I. The climatology is defined as the 20-yr (1980–99) mean of 3D temperature, moisture, cloud, and ozone fields, as well as surface pressure fields derived from the fifth major global reanalysis produced by ECMWF (ERA5) (Hersbach et al. 2020). These data are archived at the National Center for Atmospheric Research, Computational, and Information Systems Laboratory and can be downloaded online (https://doi.org/10.5065/P8GT-0R61). The horizontal spatial resolution is 1.5° longitude × 1.5° latitude. There are a total of 37 pressure levels plus the surface layer with 14 levels above 200 hPa. The model used for calculating EGK is Fu–Liou's radiation transfer model[2] (Fu and Liou 1992, 1993). The concentration levels of CO_2, CH_4, and N_2O are 352.2, 1.7, and 0.3 PPM, respectively.

[2] To avoid the mismatch between the levels and layers for energy input and output, we convert Fu–Liou's radiation model from a level model to a layer model. The conversion can be achieved by calculating LW heating rates due to downward and upward LW fluxes separately, instead of first obtaining the net downward LW fluxes and then obtaining the convergence of the net downward fluxes.

3. Physical meaning of surface amplification factor and illustration

Part I defines EGK as a matrix representing the energy gain at a given horizontal location through the coupled atmosphere–surface temperature response to unit energy perturbations (1 W m^{-2}) imposed individually at each layer, one by one. Mathematically, it is given by

$$\mathbf{G} = (G_{i,j}) = \left(\frac{\partial R_i}{\partial T_i}\right)\left(\frac{\partial R_i}{\partial T_j}\right)^{-1}, \tag{1}$$

where $(\partial R_i/\partial T_j)$ is the Planck feedback matrix (W m^{-2} K^{-1}) and $(\partial R_i/\partial T_i)$ is the diagonal matrix of $(\partial R_i/\partial T_j)$. The element at the ith row and jth column of $(\partial R_i/\partial T_j)$ represents the divergence perturbations of LW fluxes at the ith layer due to 1 K of warming from climate mean temperature at the jth layer.

For a given vertical profile of energy perturbations (ΔF_i), whether external or internal due to responses of nontemperature feedback processes to external energy perturbations, the vertical profile of the amplified energy perturbations by the EGK is

$$\Delta F_i^{\text{amplified}} = \sum_{j=1}^{L+1} G_{i,j}\Delta F_j. \tag{2}$$

The radiative equilibrium temperature change in response to ΔF_i can be obtained by requiring the LW emission perturbations of individual layers to balance the amplified energy perturbations, namely,

$$\frac{\partial R_i}{\partial T_i}\Delta T_i = \Delta F_i^{\text{amplified}}, \tag{3}$$

where ΔT_i is the temperature change at the ith layer. At a given layer i, the amplified energy perturbation ($\Delta F_i^{\text{amplified}}$) consists of two parts. One part is the amplification of the original energy perturbation at i ($G_{i,i}\Delta F_i$). The other part is the energy gained from thermal energy emission perturbations that are in radiative equilibrium with the original energy perturbations in other layers ($\sum_{j\neq i} G_{i,j}\Delta F_j$).

Figure 1 shows an example of the EGK. The diagonal elements of the EGK are always greater than the imposed unit energy perturbation in diagonal layers. The additional energy perturbations (with respect to 1 W m^{-2}) of diagonal elements correspond to the LW flux convergence perturbation in diagonal layers induced by the coupled atmosphere–surface temperature response. The off-diagonal elements of EGK are all positive, representing the energy gain from the LW flux convergence perturbations across other layers induced by the coupled atmosphere–surface temperature response to the unit forcing in diagonal layers.

The surface column ($G_{i,L+1}$), surface row ($G_{L+1,j}$), and diagonal element ($G_{i,i}$) of the EGK, where $L + 1$ denotes the surface layer and L denotes the number of atmospheric layers above the surface, represent the most information-rich vertical profiles in terms of the strength of temperature feedback in individual layers, with a focus on the surface (Fig. 2). Figure 2a

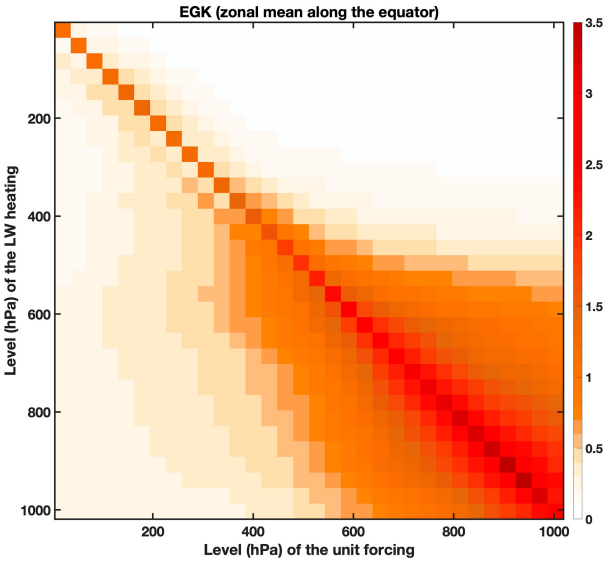

FIG. 1. The EGK derived using the vertical profile of the zonal mean fields of temperature, water vapor, and clouds along the equator. The elements of EGK are dimensionless. Their numerical values (shadings) correspond to the total energy flux convergence perturbations (W m^{-2}) at the level (hPa) indicated by the ordinate due to the coupled atmosphere–surface temperature response (or the temperature feedback) to the unit forcing (1 W m^{-2}) at the level (hPa) indicated by the abscissa.

shows the latitudinal variation of the surface column ($G_{i,L+1}$), which is the energy gain in individual layers when an energy perturbation is imposed only at the surface layer. The atmosphere–surface thermal radiative coupling is strongest in the tropics and weakest over the Antarctic, where not only is the energy amplification at the surface smallest but the atmospheric layers also gain little from the energy imposed at the surface. The surface row of EGK (Fig. 2b) represents the energy gain at the surface through the atmosphere–surface thermal radiative coupling from energy perturbations imposed at individual layers. In the tropics, energy perturbations at the midtroposphere can exert a significant influence on the surface, with the energy gain at the surface being as large as the original energy perturbation strength imposed at 700 hPa. A similar effect is found along midlatitude storm tracks, particularly in 40°–60°S where clouds are abundant. The diagonal of the EGK (Fig. 2c) is the vertical profile of the energy amplification of individual layers with respect to energy perturbations imposed at the same layers. Except for the polar regions, the largest energy amplification rate is in the lower atmospheric layers rather than at the surface. Within the tropics, the energy amplification rate of individual layers is large and relatively uniform within the entire lower troposphere, due to the tropical atmosphere being the opaquest to infrared radiation.

The ground values ($p = p_s$) in each panel of Fig. 2 represent the latitudinal variation of the surface element of EGK. This surface element, $G_{L+1,L+1}$, referred to as the SAF, represents the energy gain at the surface layer due to the energy input imposed at the surface through its thermal radiative coupling with atmospheric layers. The spatial variation of SAF reflects an important aspect of the state dependency of climate sensitivity. The latitudinal variations of energy gain by the surface layer from individual atmospheric layers (values above the ground in Fig. 2b) closely follow the latitudinal variation of SAF. Similarly, the energy gain by individual atmospheric layers from the surface (values above the ground in Fig. 2a) also follows the latitudinal variation of SAF. Therefore, understanding the spatial variation of SAF is directly applicable to the spatial variations of gain by the surface layer from individual atmospheric layers (Fig. 2b) and by individual atmospheric layers from the surface (Fig. 2a). Based on Eq. (1), SAF can be expressed as

$$\mathrm{SAF} = G_{L+1,L+1} = 1 - \sum_{k=1}^{L} \frac{\partial R_{L+1}}{\partial T_k} P_{k,L+1}, \tag{4}$$

where $P_{k,l}$ is an element in the inverse of the Planck feedback matrix, i.e., $(P_{k,l}) = (\partial R_i/\partial T_j)^{-1}$. The first term on the right-hand side of Eq. (4) represents the unit energy perturbation (1 W m^{-2}) imposed at the surface. The second term is the downward LW flux perturbation at the surface due to the air temperature warming in response to the surface warming caused directly by the imposed unit energy perturbation. It represents the energy gain at the surface from air temperature feedback in response to the original unit energy perturbation

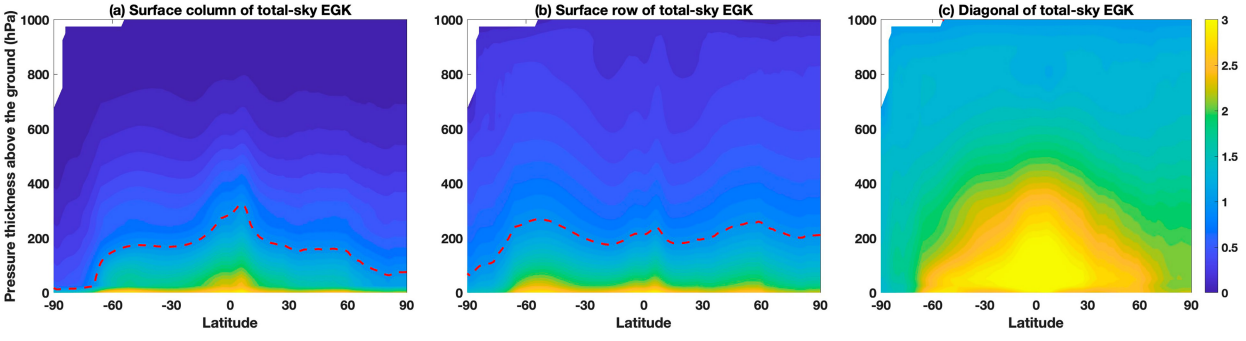

FIG. 2. Vertical–latitudinal profiles of (a) the surface column, (b) the surface row, and (c) the diagonal of the EGK derived using vertical profiles of the zonal mean fields of temperature, water vapor, and clouds from 90°S to 90°N. The vertical coordinate is the pressure thickness above the ground (hPa), equaling ($p_s - p$), where p_s is the surface pressure and p is the pressure at each level. The dashed red lines in (a) and (b) represent the contour where the value equals 1. All values in (c) exceed 1.

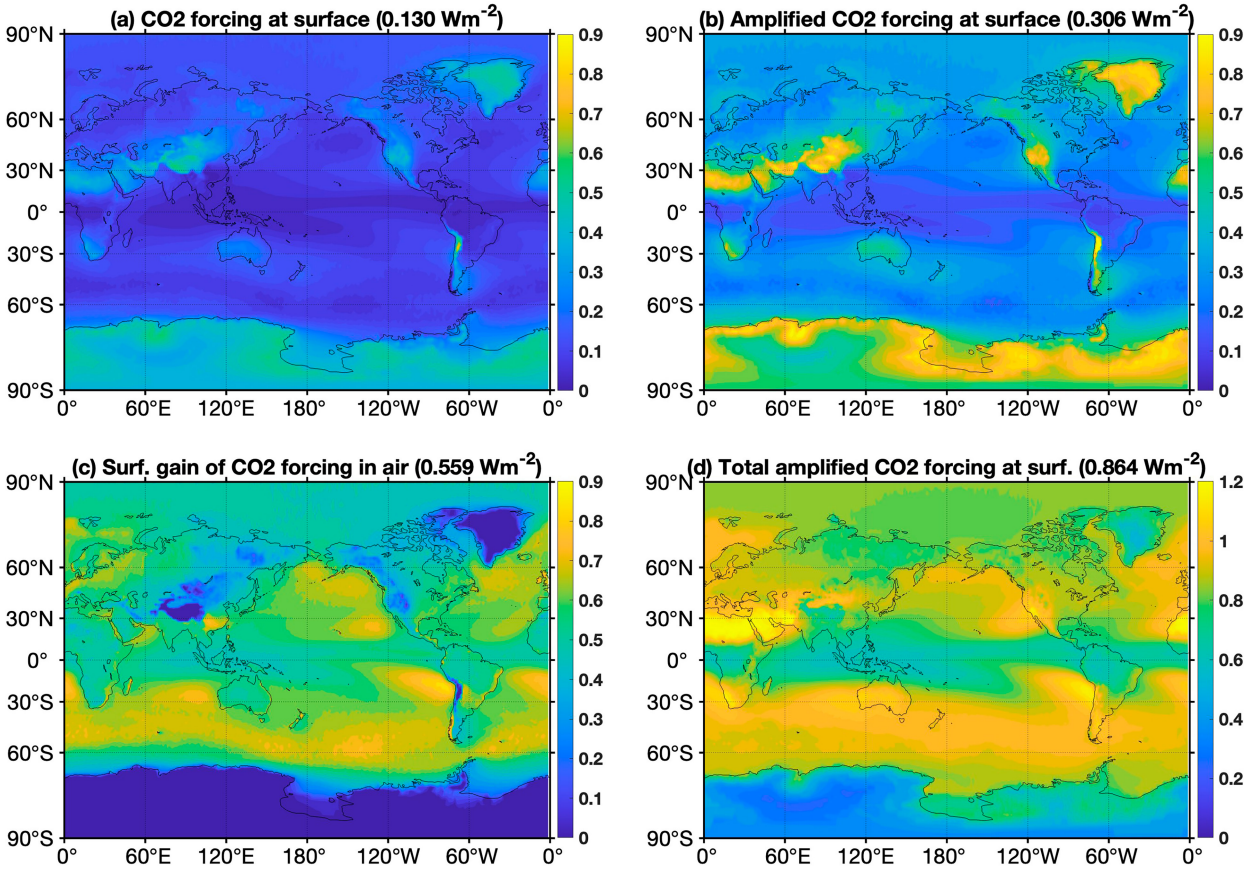

FIG. 3. Maps of (a) external energy perturbations at the surface determined from the observed increase in CO_2 concentration from 1980–2000 to 2000–20 (W m^{-2}), (b) amplified external energy perturbations at the surface (W m^{-2}), (c) energy perturbations gained at the surface from thermal energy emission perturbations in the air that are in radiative equilibrium with CO_2-induced energy perturbations in atmospheric layers (W m^{-2}), and (d) the sum of (b) and (c).

at the surface. Each term inside the summation operator, $-(\partial R_{L+1}/\partial T_{k<L+1})P_{k<L+1,L+1}$, is the contribution to the energy gain at the surface from the air temperature feedback of the kth layer. The strength of these terms is determined by the product of two positive terms: $-(\partial R_{L+1}/\partial T_{k<L+1}) > 0$ and $P_{k<L+1,L+1} > 0$. The term $P_{k<L+1,L+1}$ corresponds to the radiative equilibrium temperature response of the kth layer, as it absorbs extra energy emitted from the surface and other atmospheric layers in response to the unit energy perturbation at the surface. The term $-(\partial R_{L+1}/\partial T_{k<L+1})$ represents the contribution to the downward LW radiative flux perturbation from the kth layer per 1-K warming from the climate mean state. The value of $-(\partial R_{L+1}/\partial T_{k<L+1})$ is more positive when there are less LW absorbers or the LW optical thickness is smaller between the surface and the kth layer in the climate mean state. The strength of $P_{k<L+1,L+1}$ can be influenced by temperature and its vertical profile, besides the LW optical thickness.

Applying Eq. (2) to the surface layer, we obtain the total amplified energy perturbation at the surface:

$$\Delta F_{L+1}^{\text{amplified}} = G_{L+1,L+1}\Delta F_{L+1} + \sum_{k=1}^{L} G_{L+1,k}\Delta F_k. \qquad (5)$$

The first term on the right-hand side of Eq. (5) is the amplification of ΔF_{L+1}. The second term is energy perturbations gained at the surface from thermal energy emission perturbations in the air that are in radiative equilibrium with the original energy perturbations $\Delta F_{k<L+1}$ in the atmospheric layers. According to Eq. (5), $G_{L+1,k}\ \Delta F_k$, for $k < L + 1$, measures the strength of the energy gain at the surface from energy perturbations at the kth atmospheric layer.

Figure 3 provides an example of the amplification of radiative forcing due to an increase in CO_2 concentration from 352.2 ppm during 1980–2000 to 385 ppm during 2000–20. Figure 3a illustrates the spatial pattern of instantaneous CO_2 forcing at the surface (ΔF_{L+1}). Larger values of ΔF_{L+1} are over elevated areas and deserts where climate mean water vapor is scarce. This scarcity reduces the spectral overlap between CO_2 and water vapor, allowing more downward LW radiative fluxes to reach the surface. Conversely, regions with more moisture, such as the tropics, exhibit smaller values of ΔF_{L+1} due to greater spectral overlap and absorption of LW radiation by water vapor (Hu et al. 2017a, 2018). The surface's thermal emission increases in response to surface warming from the instantaneous forcing. This additional emission is

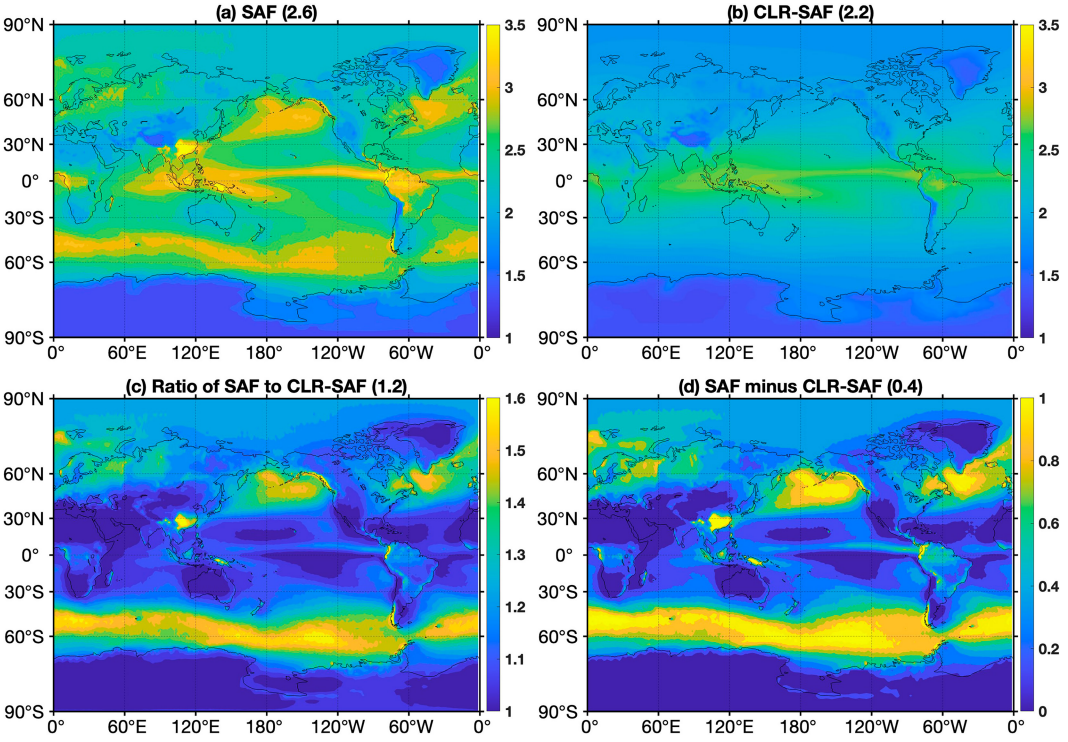

FIG. 4. Maps of (a) SAF, (b) clear-sky SAF (CLR-SAF), (c) the ratio of (a) to (b), and (d) the difference between (a) and (b). The number in the title of each panel represents the global mean value. CLR-SAF is obtained similarly to SAF, except that values of climate mean clouds are set to zero during the radiative transfer model calculation.

absorbed by the atmosphere, leading to atmospheric warming. The atmospheric warming results in positive downward thermal LW perturbations, amplifying the CO_2-induced energy perturbations at surface ($G_{L+1,L+1}\Delta F_{L+1}$ in Fig. 3b). The ratio of Fig. 3b to Fig. 3a is SAF, which is the main focus of the remaining part of the paper. Over the regions where climate mean state is moist and/or cloudy, CO_2-induced energy perturbations in the lower atmospheric layers ($\Delta F_{k<L+1}$) are much stronger than at the surface (ΔF_{L+1}). This is due to the spectral overlap between CO_2 and water vapor. Values of $G_{L+1,k<L+1}$ are also higher in these moist and/or cloudy regions compared to drier regions. As a result, energy perturbations gained at the surface through the enhanced downward LW flux emitted from warmer air are greater over moist and/or cloudy regions ($\sum_{k=1}^{L} G_{L+1,k}\Delta F_k$ in Fig. 3c). At the equator, the CO_2-induced energy perturbations are largest in the lower to midtroposphere, rather than at the surface. However, because of the high opacity, only a small fraction of the downward LW emission perturbations from CO_2-induced air warming passes through the lower troposphere to reach the surface. This explains the generally weak gain of energy at the surface from the CO_2-induced energy perturbations in the atmosphere along the equatorial band (Fig. 3c). The differences between Fig. 3b and Fig. 3a and between Fig. 3c and Fig. 3a are attributed to air temperature feedback in response to CO_2-induced energy perturbations. The sum of Fig. 3b and Fig. 3c represents the total energy perturbations at the surface, i.e., $\Delta F_{L+1}^{\text{amplified}}$ given in Eq. (5), due to the increase in CO_2 (Fig. 3d). This total energy perturbation determines the surface temperature warming, according to $\Delta T_{L+1} = F_{L+1}^{\text{amplified}}/(\partial R_{L+1}/\partial T_{L+1})$, in the absence of nontemperature feedbacks.

4. SAF spatial pattern and its dependence on LW absorbers in the atmosphere

The spatial pattern of SAF is shaped collectively by the nonuniform spatial distributions of atmospheric LW absorbers in the climate mean state, as well as surface temperature T_S. The climate mean variables that directly affect nonuniform distributions of atmospheric LW absorbers include surface pressure, water vapor, and clouds. In this section, we will examine how SAF depends on the climate mean fields of surface pressure, water vapor, and clouds.

The spatial pattern of SAF (Fig. 4a) closely resembles the climate mean cloud field (Fig. 5a), with the maximum value exceeding 4 over the western Pacific warm pool region. Over midlatitude storm-track regions, SAF values range from 2.9 to 3.2, which are higher than those over subtropical oceans, where they range from 2.2 to 2.6. Over the polar regions, SAF values range from 2.0 to 2.8 over the Arctic Ocean but only from 1.4 to 1.7 over the Antarctic continent. Additionally, SAF tends to have minimum values over Antarctica and high-elevated areas, such as the Tibetan Plateau, Andes, Rockies, and Greenland. The minimum SAF values over high-elevated areas result from the scarcity of LW absorbers. This scarcity is directly due to the lack of water vapor (Fig. 5c) because

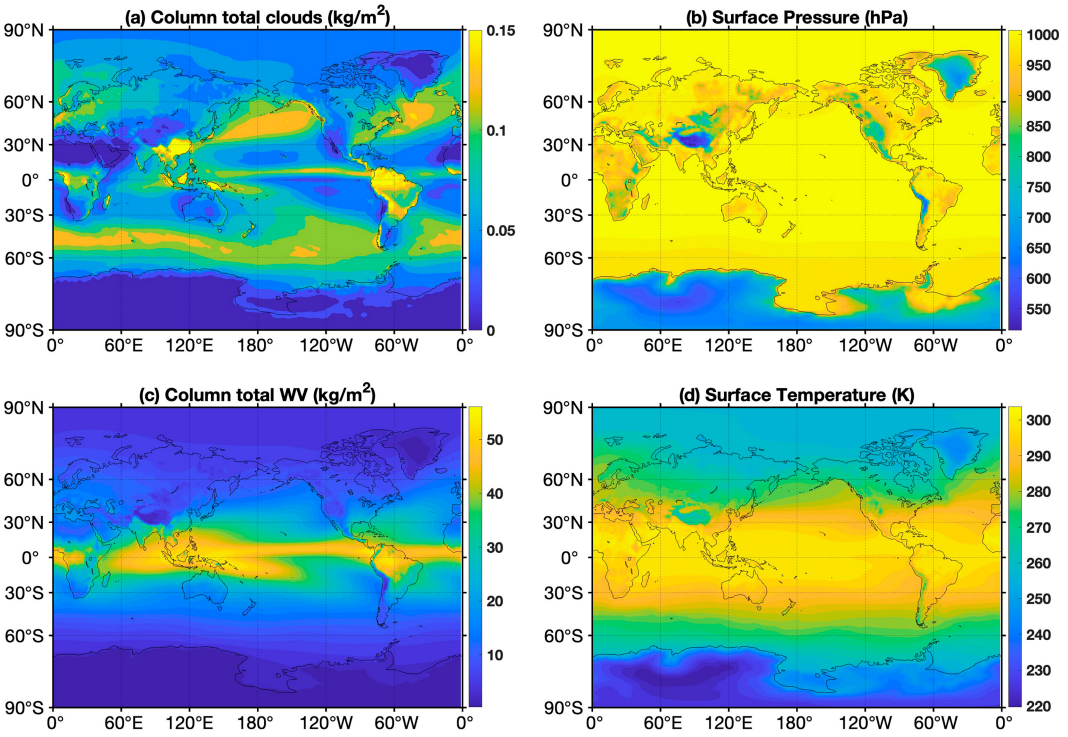

FIG. 5. Maps of climatological (a) column-integrated liquid and ice cloud water content (kg m^{-2}), (b) surface pressure (hPa), (c) column-integrated water vapor (kg m^{-2}), and (d) surface temperature (T_S; K) in the period from 1980 to 1999.

of low T_S (Fig. 5d). The indirect factor for the lack of LW absorbers is low surface pressure over high-elevated areas (Fig. 5b), as it implies less air mass above the ground and consequently less well-mixed gas absorbers (Feng et al. 2023). Compared to Antarctica, the larger SAF values over the Arctic can be attributed to higher surface pressure and relatively abundant moisture in that region.

To isolate the contribution of water vapor to the strength of SAF from that of clouds, we calculated SAF under clear-sky conditions, denoted as CLR-SAF (Fig. 4b). It is seen from Fig. 4b that CLR-SAF tends to decrease with latitude, with maximum values along the intertropical convergence zone (ITCZ). These maximum values of CLR-SAF along ITCZ closely overlap with regions of high climatological water vapor content (Fig. 5c). Figure 6b shows that CLR-SAF generally increases with higher column-integrated water vapor and T_S. Because of the Clausius–Clapeyron relation, water vapor content tends to follow temperature in observations. Thus, the positive correlation with T_S shown in Fig. 6b mainly reflects the positively correlated relationship between SAF and the amount of LW absorbers in the atmosphere, i.e., the climate mean water vapor content in this case.

The magnitude of SAF is noticeably greater than CLR-SAF, particularly outside the tropics. Over Antarctic, SAF and CLR-SAF are about the same due to the scarcity of climate mean cloud cover. The global mean value of SAF is about 2.6, which is 18% greater than the global mean of CLR-SAF. The difference between SAF and CLR-SAF reflects that the strength of SAF increases with the amount of LW absorbers (i.e., clouds in this case). Unlike CLR-SAF, large values of SAF exceeding 3 are also found over storm-track regions in the North Pacific, Atlantic, and South Ocean. In these regions, the effect of climate mean clouds accounts for a 40%–60% increase in SAF values (Fig. 4c). The ratio between SAF and CLR-SAF, as well as their differences (Fig. 4d), is significantly larger over midlatitude storm-track regions compared to tropical regions. As a result, SAF over midlatitude storm-track regions is as large as that over the ITCZ in the tropics (Fig. 4b), despite the much lower water vapor content. Also, the presence of clouds over Arctic leads to about a 20%–30% increase in SAF values compared to CLR-SAF. Therefore, the climate mean cloud field largely shapes the spatial pattern of SAF, particularly outside the tropics, even though the climate mean column-integrated cloud water content is less than 0.5% of the climate mean column-integrated water vapor content.

5. Dependence of SAF on surface temperature

The comparison between Figs. 4a and 4b and Fig. 5d reveals that the spatial pattern of T_S does not play a major role in shaping the spatial patterns of both CLR-SAF and SAF. However, a close inspection of the scatterplot in Fig. 6b reveals two separated branches of data points when T_S is below 290 K. The two separated branches are also evident in Fig. 6a when the column-integrated water vapor is below 20 kg m^{-2}.

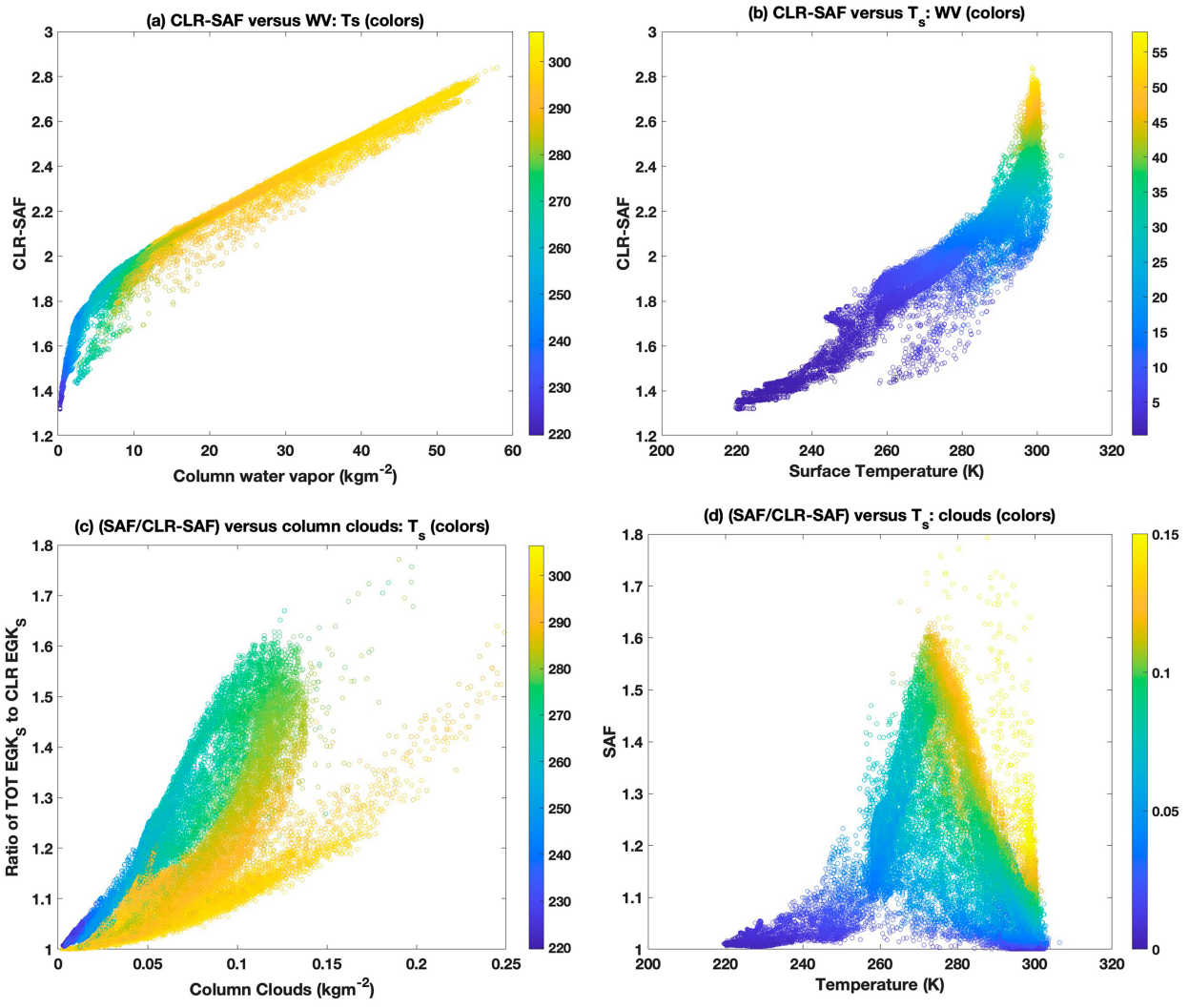

FIG. 6. Scatterplots of (a) clear-sky SAF vs climate mean column-integrated water vapor (kg m^{-2}) color coded by climate mean T_S (K), (b) CLR-SAF vs climate mean T_S color coded by climate mean column-integrated water vapor (kg m^{-2}), (c) the ratio of SAF to CLR-SAF vs climate mean column-integrated clouds (kg m^{-2}) color coded by T_S (K), and (d) the ratio of SAF to CLR-SAF vs climate mean T_S (K) color coded by column-integrated clouds (kg m^{-2}).

The comparison between these two branches in Fig. 6a indicates that for the same amount of water vapor content, the upper branch has larger CLR-SAF values with colder T_S, but the lower branch has smaller CLR-SAF values with warmer T_S. There are also multiple branches of data points in the scatterplot of the ratio of SAF to CLR-SAF against column-integrated clouds (Fig. 6c), although the width of these branches is greater than those in Figs. 6a and 6b. Figure 6c shows that the ratio of SAF to CLR-SAF increases more rapidly with column-integrated clouds at lower T_S compared to higher T_S. The existence of multiple branches with different slopes in Fig. 6c implies that for the same amount of column-integrated clouds, the ratio of SAF to CLR-SAF tends to increase as T_S decreases. This suggests a negative correlation between SAF and T_S. Figure 6d indicates that this negative correlation relationship emerges when the cloud content is abundant.

The dependence of SAF on T_S is complex because it is jointly determined by thermal emission spectrum and absorption spectrum, both of which are sensitive to temperature. According to Wien's law, the wavelength of peak emission radiance is inversely proportional to temperature. As a result, the alignment of the peak thermal emission radiance with the atmospheric absorption bands becomes temperature dependent. Moreover, per Stefan–Boltzmann law, the overall emission (i.e., spectrally integrated emission) is proportional to the fourth power of temperature. Therefore, the overall emission effect also causes the atmospheric absorption strength to depend on the amount of LW absorbers differently at different temperatures. It is the atmosphere's absorption of LW energy emitted from the surface that initiates the amplification of energy perturbations at the surface through air temperature feedback. Therefore, these two opposing dependencies of

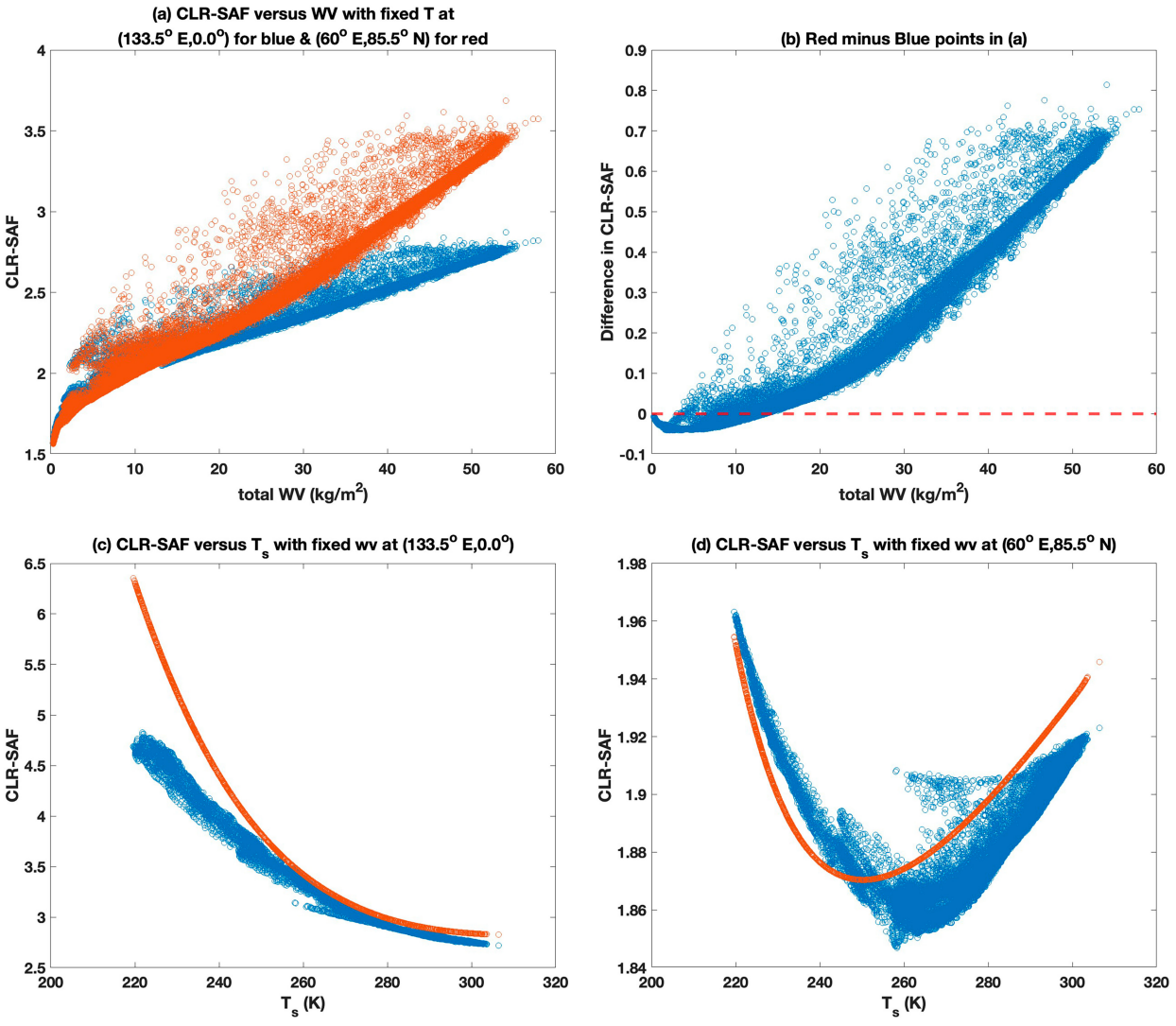

FIG. 7. Scatterplots of (a) clear-sky SAF vs climate mean column-integrated water vapor (kg m^{-2}) with fixed temperature profile taken at (0°, 133.5°E) for blue points and at (85°N, 60°E) for red points, (b) difference in clear-sky SAF between red and blue points in (a), clear-sky SAF vs climate mean surface temperature (K) with the fixed water vapor profile taken at (c) (0°, 133.5°E) and at (d) (85°N, 60°E). The red curves in (c) and (d) are obtained using vertical uniform temperature profiles that are equal to the local surface temperatures.

emission properties on temperature imply that the dependence of SAF on T_S is expected to vary with the quantity of LW absorbers in the atmosphere.

To confirm this conjecture, we repeat the same calculation of CLR-SAF shown in Figs. 6a and 6b but using two fixed temperature profiles: one from (0°, 133.5°E), representing warmer temperatures, and the other from (85°N, 60°E), representing colder temperatures. This approach allows us to mimic the existence of multiple branches of data points with different slopes depending on T_S shown in Figs. 6a and 6d. The results presented in Fig. 7a reproduce the multiple branches of data points in the scatterplot of SAF versus LW absorbers. Specifically, the scatterplot obtained using the warmer temperature (blue points) exhibits a slower increase in CLR-SAF with column-integrated water vapor compared to the colder temperature profile (red points). Their differences (Fig. 7b) indicate that CLR-SAF values obtained with the colder temperature profile are generally higher than those obtained with the warmer temperature profile. However, when column-integrated water vapor is very scarce, CLR-SAF values obtained with the warmer temperature profile can be greater. These results suggest that SAF tends to correlate negatively with T_S when atmospheric LW absorbers are abundant but positively when they are scarce.

To further confirm that the sign of SAF–T_S correlation strongly depends on the amount of atmospheric LW absorbers, we repeated the CLR-SAF calculation shown in Figs. 6a and 6b using two fixed water vapor profiles: one from (0°, 133.5°E), representing very abundant water vapor, and the other from (85°N, 60°E), representing modestly abundant

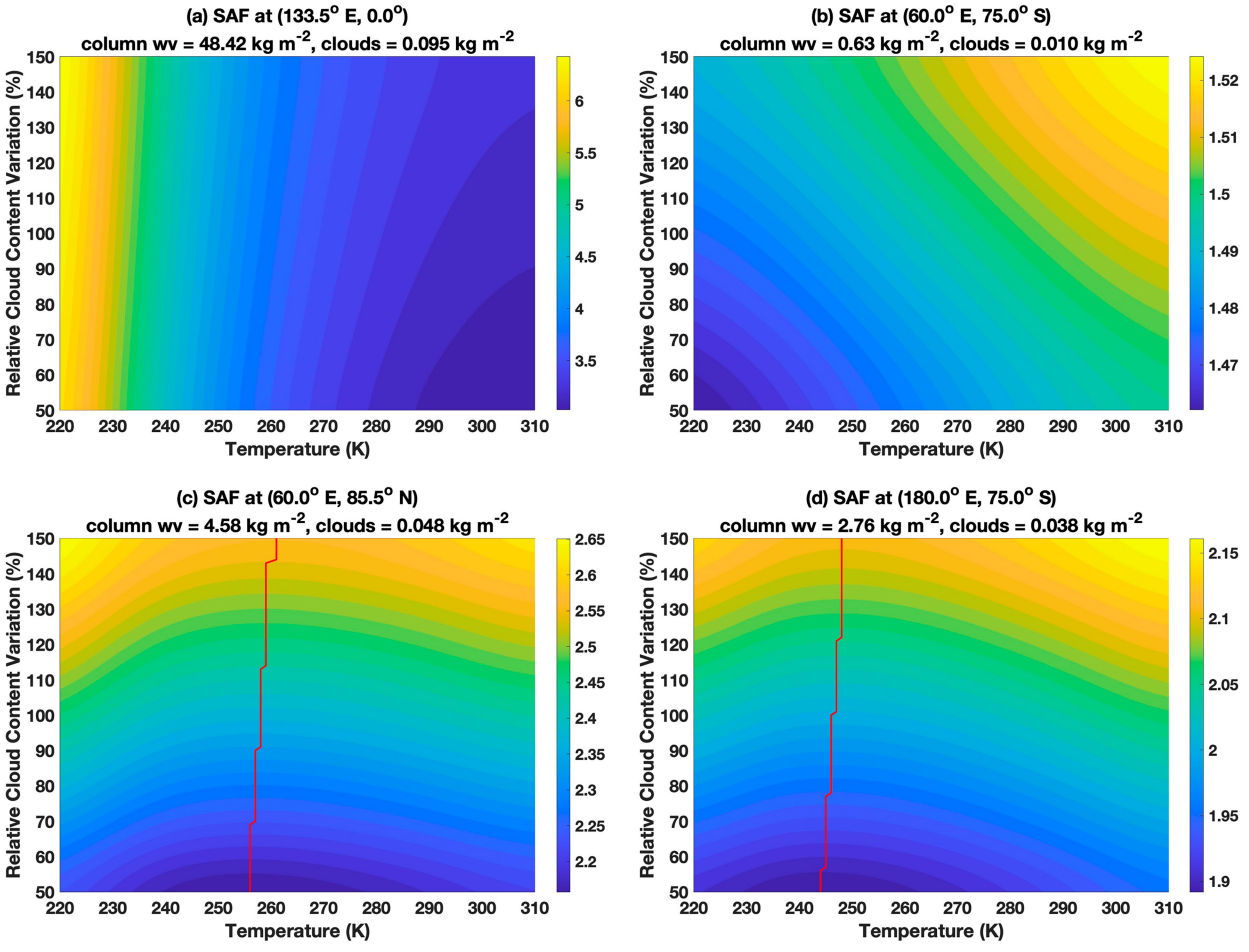

FIG. 8. Variation of SAF (shadings) as a function of the amount of LW absorbers in the atmosphere (ordinate) and (vertically uniform) temperature (K; abscissa) with the reference absorber level set at (a) (0°, 133.5°E), (b) (75°S, 60°E), (c) (85.5°N, 60°E), and (d) (75.5°S, 180°). The reference absorber level (kg m^{-2}) is given in the second line of each panel's title. The amount of LW absorbers is equal to the sum of the reference column water vapor amount and the product of the reference cloud amount and the percentage values provided on the label for ordinate. The red line in (c) and (d) marks the minimum point of SAF for each level of cloud content.

water vapor. The result displayed in Fig. 7c clearly indicates that SAF tends to decrease with T_S when atmospheric LW absorbers are very abundant. When atmospheric LW absorbers are modestly abundant, such as over the Arctic, SAF tends to decrease with T_S in colder conditions but increase with T_S in warmer conditions (Fig. 7d). The result obtained with the water vapor profile taken at (75°S, 60°E), where water vapor is very scarce, indicates that SAF increases with T_S monotonically when atmospheric LW absorbers are scarce (see Fig. 8b).

To explicitly delineate the complex SAF–T_S relation that varies with the quantity of LW absorbers in the atmosphere, we conducted a series of sensitivity calculations of SAF under different combinations of temperature and amount of LW absorbers in the atmosphere at four representative locations (Fig. 8). To minimize the complication from vertically varying temperatures, all sensitivity calculations were conducted using vertically uniform temperature profiles, with temperature ranging from 220 to 310 K. We use the observed profiles of water vapor and clouds at the following four locations: (0°, 133.5°E), representing the case of very abundant LW absorbers in the atmosphere located in the equatorial warm pool region; (75°S, 60°E), representing very scarce LW absorbers over western Antarctica; and (85.5°N, 60°E) and (75°S, 189°E), representing dry but cloudy conditions over polar marine environments. Because the cloud content is not as closely correlated with temperature as water vapor, we vary the cloud content from 50% to 150% of the observed cloud content at these four locations. This approach allows to illustrate how the strength of SAF varies with T_S under varying levels of LW absorbers in the atmosphere.

It is evident from Fig. 8a that the strength of SAF decreases with temperature when LW absorbers in the atmosphere are very abundant, such as in the equatorial warm pool region with high water vapor content. Conversely, the strength of SAF increases with T_S when LW absorbers are scarce, as seen over the high elevated western Antarctic continent with extremely low water vapor content (Fig. 8b). According to Wien's law, the thermal energy emitted from the surface at

higher temperature peaks at shorter wavelengths. The shift of the peak emission's wavelength toward a longer wavelength at lower temperatures results in more alignment with atmospheric absorption bands. Consequently, the atmosphere can absorb more thermal energy emitted from the surface at lower temperatures, as long as LW absorbers are abundant. The more LW absorption by the atmosphere leads to stronger warming. This in turns leads to more downward thermal energy fluxes, amplifying surface energy perturbations more strongly. Consequently, SAF exhibits a negative correlation with T_S when LW absorbers are abundant.

When LW absorbers are below the "abundance" condition, the overall emission effect, namely, a warmer surface emits more thermal energy than a colder one, becomes dominant over the wavelength shift effect. As a result, an atmosphere with scarce LW absorbers would absorb more thermal energy emitted from the surface at a warmer surface compared to a colder one, despite the relatively lesser alignment of the peak emission wavelength with atmospheric absorption bands. This explains why SAF exhibits a positive correlation with T_S when LW absorbers are scarce.

Figures 8c and 8d reveal that SAF tends to first decrease with T_S and then increase when LW absorbers are modest. The threshold abundance of LW absorbers, which separates a negative correlation of SAF with T_S from a positive one, decreases as T_S decreases, as indicated by red lines in Figs. 8c and 8d. Moreover, the threshold temperature for separating positive and negative correlations of SAF with T_S decreases as the quantity of LW absorbers decreases (comparing Fig. 8c to Fig. 8d). As a result, as the quantity of LW absorbers increases, the negative correlation regime of SAF with T_S becomes dominant (Fig. 8a), while the positive correlation regime prevails when LW absorbers are very scarce (Fig. 8b).

It is important to point out that the vertical structure of both LW absorbers and temperature also complicate the SAF–T_S relation. The red scatterplots in Figs. 7c and 7d are obtained in the same manner as the corresponding blue scatterplots. However, the actual vertical profiles of temperatures are replaced with vertically uniform temperature profiles equal to the local T_S. As seen in Fig. 8, using vertically uniform temperature results in scatterplots becoming curve plots. The differences between curves and the corresponding scatterplots indicate that air temperatures, which are colder than T_S, tend to weaken the negative slope of the SAF–T_S relation under conditions of abundant LW absorbers and slightly strengths the positive slope under conditions of less abundant LW absorbers. Because of the great spatial variability of atmospheric lapse rates, the SAF–T_S relation becomes somewhat blurred, with slight adjustments in its slopes. Nevertheless, since both water vapor and temperature tend to decrease with height and follow T_S, their vertical variations only have a limited impact on the SAF–T_S relationship. However, clouds exhibit varying vertical structures across different regions. This variability causes the multiple branches of data points with temperature-dependent slopes shown in Fig. 6c to spread out more compared to Fig. 6a. Therefore, the high variability in clouds largely masks the SAF–T_S relationship in the spatial pattern of SAF.

The Clausius–Clapeyron relation sets an upper limit on the amount of water vapor at a given temperature. As a result, it is rare for the negative SAF–T_S relationship to become dominant under clear-sky condition, as water vapor content always decreases with decreasing temperature. In other words, the abundance condition for LW absorbers rarely occurs under clear-sky conditions. However, the amount of cloud content in the air is not directly related to temperature. Therefore, the abundance condition of LW absorbers (i.e., clouds) can occur over a much wider range of temperatures, extending from cold to modest temperatures. This explains why SAF can be greater over colder regions, such as midlatitude storm-track regions, compared to warmer regions like the tropics (Fig. 4). Despite the pronounced low levels of water vapor and cloud content in the Arctic compared to the tropics, SAF in the Arctic still falls within the range of 2.2–2.9 (Fig. 4a), which is about 70%–90% of SAF in the tropics. In contrast, CLR-SAF in the Arctic is no more than 70% of CLR-SAF in the tropics (Fig. 4b). Therefore, because of the temperature effect (i.e., the temperature dependence of the alignment of the peak thermal emission radiance with atmospheric absorption bands), the climate mean cloud content plays an important role in shaping the spatial pattern of SAF outside the tropics.

6. Conclusions and discussion

In Part I of the three-series papers, we presented a new climate feedback kernel, referred to as the "energy gain kernel" (abbreviated as "EGK") based on the radiative transfer principles. The EGK encapsulates the positive aspect of temperature feedback, whereas the diagonal matrix of the Planck feedback matrix encapsulates the negative aspect. Elements of the EGK correspond to thermal radiative energy flux convergence perturbations at individual layers, resulting from the coupled atmosphere–surface temperature changes in response to unit forcing in each layer. Mathematically, the EGK represents the analytical (linearized) equilibrium solution of climate models in response to input energy perturbations, considering only temperature feedback. The equilibrium solution represented by EGK is expressed as the amplification of input energy perturbations at the layers where input energy is located and gains of energy by other layers, rather than as the warmings at individual layers. The strength of the EGK depends collectively on climate mean temperature, water vapor, clouds, and surface pressure. It acts to amplify any input energy perturbations imposed to a climate system.

We examine the spatial pattern of the EGK derived from observations and its relationships with spatial variations in variables affecting the climate mean infrared opacity across atmospheric layers, namely, water vapor, clouds, surface pressure, and climate mean surface temperature T_S. At a given horizontal location, the EGK is a two-dimensional matrix. The column and row indices of this matrix correspond to, respectively, the layer where input energy perturbations are introduced and the layer where energy is gained in response to input energy perturbations through temperature feedback. While the spatial patterns of each element of the EGK differ, they generally align with the spatial pattern of the surface

element of the EGK. The surface element represents the amplification of input energy perturbations at the surface by (air) temperature feedback, referred to as the surface amplification factor (SAF). At a given location, the SAF's amplification effect on input energy perturbations at the surface is identical, regardless of the perturbations' origins (i.e., external or internal due to nontemperature feedbacks), their strength, and their sign. Therefore, understanding the spatial variation of SAF could provide valuable insights into the spatial variability of climate sensitivity.

In general, the more longwave (LW) absorbers in the atmosphere, the greater SAF. SAF tends to be higher in regions with abundant atmospheric water vapor, such as the tropics, the tropical intertropical convergence zone (ITCZ), and midlatitude storm tracks where clouds are prevalent. The global mean value of SAF is about 2.6. The spatial pattern of SAF closely resembles that of climate mean cloud field, with maximum values exceeding 4 over the western equatorial pacific warm pool region. In midlatitude storm-track regions, the strength of total-sky SAF ranges from 2.9 to 3.2, which is greater than the subtropical oceans, where it ranges from 2.2 to 2.6. Over the Arctic Ocean, the strength of total-sky SAF ranges from 2.0 to 2.8, whereas over the Antarctic continent, it only ranges from 1.4 to 1.7. The amount of LW absorbers in the atmosphere is also significantly influenced by topography and surface pressure. Low surface pressure over highly elevated regions results in fewer LW absorbers, leading to smaller values of SAF. This factor alone could partially explain the much weaker climate sensitivity over the Antarctic continent compared to the Arctic Ocean.

The dependency of SAF on T_S is somewhat complicated. On the one hand, the column-integrated water vapor tends to follow T_S closely because of the Clausius–Clapeyron relation. As a result, the strength of clear-sky SAF appears proportional to T_S. In the tropics, the presence of abundant clouds only slightly increases SAF due to absorption saturation caused by the abundance of water vapor. Outside the tropics, where water vapor is less abundant, clouds substantially elevate the strength of SAF. Note that T_S decreases with latitude, but the amount of clouds does not. Consequently, the strength of SAF appears to both increase and decrease with T_S in the scatterplot of SAF against T_S. This varying dependence of SAF on T_S likely reflects its dependence on cloud amount rather than a direct dependence on T_S itself. This factor may partly explain the varying dependency of climate sensitivity on climate mean temperature found in climate models as reviewed in introduction. For example, models with more clouds in cold places would have a larger climate sensitivity due to greater SAF than models with fewer clouds in cold places, despite the colder climate mean temperature of the former.

In this study, we provide theoretical evidence suggesting that SAF indeed can vary with T_S differently, even under the same amount of LW absorbers. Because the wavelength of peak emission radiance is inversely related to temperature, the alignment of the peak thermal emission radiance with atmospheric absorption bands becomes temperature dependent. Furthermore, the overall emission is proportional to the fourth power of temperature. This overall emission effect can also cause the atmospheric absorption strength to depend on the amount of LW absorbers differently at different temperatures. These two opposing dependencies of emission properties on temperature imply that the dependence of SAF on T_S is expected to vary with the quantity of LW absorbers in the atmosphere.

We find that SAF tends to decrease with temperature first and then begins to increase with temperature when LW absorbers in the atmosphere are modest. The threshold temperature for separating positive and negative correlations of SAF with temperature decreases as LW absorbers become less abundant. As a result, as LW absorbers increase, the negative correlation regime of SAF with temperature becomes dominant, and conversely, the positive correlation regime becomes dominant when LW absorbers are scarce.

Whether SAF is positively or negatively correlated with T_S depends on the abundance level of LW absorbers in the atmosphere. Although T_S plays a secondary role in shaping the spatial pattern of SAF, this varying dependence of SAF on T_S could partially explain why the climate sensitivity in climate models can exhibit both positive and negative temperature dependence. For example, two climate models may both show abundant clouds and water vapor over the Arctic, but one has a colder mean surface temperature while the other has a warmer mean surface temperature. Because of the abundance condition, this scenario corresponds to the negative correlation between SAF and surface temperature. In this scenario, therefore, the model with a colder Arctic is expected to exhibit larger climate sensitivity due to a stronger SAF, leading to greater Arctic warming amplification. Conversely, the scenario that two models have the same scarcity of LW absorbers over the Arctic corresponds to the positive correlation between SAF and surface temperature. In this scenario, the model with a warmer Arctic is expected to exhibit larger climate sensitivity due to a stronger SAF.

Finally, we wish to point out that one can calculate EGK from the mean climate states of climate models in the same manner as from reanalysis, provided that the output fields of these mean climate states archived in climate centers include all required input fields for a radiative transfer model. In a future study, we plan to analyze how the intermodel spread of SAF, including its strength and spatial pattern, relates to the intermodel spreads of climate mean LW absorbers and T_S. This may help us understand how the intermodel spread of climate mean states contributes to the intermodel spread of global warming projections.

Acknowledgments. The authors are in debt to the two anonymous reviewers whose constructive comments and suggestions help improve the presentation greatly. X. Hu was supported by the National Natural Science Foundation of China (42222502). M. Cai and J. Sun were in part supported by grants from the National Science Foundation (AGS-2032542 and AGS-2202875) and the Climate Program Office of National Oceanic and Atmospheric Administration (NA20OAR4310380).

Data availability statement. The ERA5 reanalysis is downloaded at https://doi.org/10.5065/P8GT-0R61. Upon request, all model codes and data analysis codes will be made available to researchers interested in reproducing the results. The authors declare no competing interests.

REFERENCES

Anagnostou, E., and Coauthors, 2020: Proxy evidence for state-dependence of climate sensitivity in the Eocene greenhouse. *Nat. Commun.*, **11**, 4436, https://doi.org/10.1038/s41467-020-17887-x.

Andrews, T., and M. J. Webb, 2018: The dependence of global cloud and lapse rate feedbacks on the spatial structure of tropical Pacific warming. *J. Climate*, **31**, 641–654, https://doi.org/10.1175/JCLI-D-17-0087.1.

Beer, E., and I. Eisenman, 2022: Revisiting the role of the water vapor and lapse rate feedbacks in the Arctic amplification of climate change. *J. Climate*, **35**, 2975–2988, https://doi.org/10.1175/JCLI-D-21-0814.1.

Bjordal, J., T. Storelvmo, K. Alterskjær, and T. Carlsen, 2020: Equilibrium climate sensitivity above 5°C plausible due to state-dependent cloud feedback. *Nat. Geosci.*, **13**, 718–721, https://doi.org/10.1038/s41561-020-00649-1.

Bloch-Johnson, J., M. Rugenstein, M. B. Stolpe, T. Rohrschneider, Y. Zheng, and J. M. Gregory, 2021: Climate sensitivity increases under higher CO_2 levels due to feedback temperature dependence. *Geophys. Res. Lett.*, **48**, e2020GL089074, https://doi.org/10.1029/2020GL089074.

Boeke, R. C., P. C. Taylor, and S. A. Sejas, 2021: On the nature of the Arctic's positive lapse-rate feedback. *Geophys. Res. Lett.*, **48**, e2020GL091109, https://doi.org/10.1029/2020GL091109.

Caballero, R., and M. Huber, 2013: State-dependent climate sensitivity in past warm climates and its implications for future climate projections. *Proc. Natl. Acad. Sci. USA*, **110**, 14 162–14 167, https://doi.org/10.1073/pnas.1303365110.

Cai, M., and J. Lu, 2009: A new framework for isolating individual feedback processes in coupled general circulation climate models. Part II: Method demonstrations and comparisons. *Climate Dyn.*, **32**, 887–900, https://doi.org/10.1007/s00382-008-0424-4.

——, J. Sun, F. Ding, W. Kang, and X. Hu, 2023: The quasi-linear relation between planetary outgoing longwave radiation and surface temperature: A climate footprint of radiative and nonradiative processes. *J. Atmos. Sci.*, **80**, 2131–2146, https://doi.org/10.1175/JAS-D-22-0261.1.

——, X. Hu, J. Sun, J. Feng, and F. Ding, 2024: Energy gain kernel for climate feedbacks. Part I: Formulation and physical understanding. *J. Atmos. Sci.*, **81**, 1033–1047, https://doi.org/10.1175/JAS-D-23-0148.1.

Colman, R., and B. McAvaney, 2009: Climate feedbacks under a very broad range of forcing. *Geophys. Res. Lett.*, **36**, L01702, https://doi.org/10.1029/2008GL036268.

——, and B. J. Soden, 2021: Water vapor and lapse rate feedbacks in the climate system. *Rev. Mod. Phys.*, **93**, 045002, https://doi.org/10.1103/RevModPhys.93.045002.

Feng, J., D. Paynter, and R. Menzel, 2023: How a stable greenhouse effect on Earth is maintained under global warming. *J. Geophys. Res. Atmos.*, **128**, e2022JD038124, https://doi.org/10.1029/2022JD038124.

Forster, P., and Coauthors, 2021: The Earth's energy budget, climate feedbacks, and climate sensitivity. *Climate Change 2021: The Physical Science Basis*, V. Masson-Delmotte et al., Eds., Cambridge University Press, 923–1054.

Fu, Q., and K. N. Liou, 1992: On the correlated *k*-distribution method for radiative transfer in nonhomogeneous atmospheres. *J. Atmos. Sci.*, **49**, 2139–2156, https://doi.org/10.1175/1520-0469(1992)049<2139:OTCDMF>2.0.CO;2.

——, and ——, 1993: Parameterization of the radiative properties of cirrus clouds. *J. Atmos. Sci.*, **50**, 2008–2025, https://doi.org/10.1175/1520-0469(1993)050<2008:POTRPO>2.0.CO;2.

Hansen, J., M. Sato, G. Russell, and P. Kharecha, 2013: Climate sensitivity, sea level and atmospheric carbon dioxide. *Philos. Trans. Roy. Soc.*, **A371**, 20120294, https://doi.org/10.1098/rsta.2012.0294.

He, H., R. J. Kramer, B. J. Soden, and N. Jeevanjee, 2023: State dependence of CO_2 forcing and its implications for climate sensitivity. *Science*, **382**, 1051–1056, https://doi.org/10.1126/science.abq6872.

Hersbach, H., and Coauthors, 2020: The ERA5 global reanalysis. *Quart. J. Roy. Meteor. Soc.*, **146**, 1999–2049, https://doi.org/10.1002/qj.3803.

Hu, X., Y. Li, S. Yang, Y. Deng, and M. Cai, 2017a: Process-based decomposition of the decadal climate difference between 2002–13 and 1984–95. *J. Climate*, **30**, 4373–4393, https://doi.org/10.1175/JCLI-D-15-0742.1.

——, P. C. Taylor, M. Cai, S. Yang, Y. Deng, and S. Sejas, 2017b: Inter-model warming projection spread: Inherited traits from control climate diversity. *Sci. Rep.*, **7**, 4300, https://doi.org/10.1038/s41598-017-04623-7.

——, M. Cai, S. Yang, and S. A. Sejas, 2018: Air temperature feedback and its contribution to global warming. *Sci. China Earth Sci.*, **61**, 1491–1509, https://doi.org/10.1007/s11430-017-9226-6.

——, H. Fan, M. Cai, S. A. Sejas, P. Taylor, and S. Yang, 2020: A less cloudy picture of the inter-model spread in future global warming projections. *Nat. Commun.*, **11**, 4472, https://doi.org/10.1038/s41467-020-18227-9.

Lu, J., and M. Cai, 2009: A new framework for isolating individual feedback processes in coupled general circulation climate models. Part I: Formulation. *Climate Dyn.*, **32**, 873–885, https://doi.org/10.1007/s00382-008-0425-3.

——, and ——, 2010: Quantifying contributions to polar warming amplification in an idealized coupled general circulation model. *Climate Dyn.*, **34**, 669–687, https://doi.org/10.1007/s00382-009-0673-x.

Martínez-Botí, M. A., and Coauthors, 2015: Plio-Pleistocene climate sensitivity evaluated using high-resolution CO_2 records. *Nature*, **518**, 49–54, https://doi.org/10.1038/nature14145.

Mauritsen, T., and Coauthors, 2019: Developments in the MPI-M Earth System Model version 1.2 (MPI-ESM1.2) and its response to increasing CO_2. *J. Adv. Model. Earth Syst.*, **11**, 998–1038, https://doi.org/10.1029/2018MS001400.

McKim, B. A., N. Jeevanjee, and G. K. Vallis, 2021: Joint dependence of longwave feedback on surface temperature and relative humidity. *Geophys. Res. Lett.*, **48**, e2021GL094074, https://doi.org/10.1029/2021GL094074.

Meraner, K., T. Mauritsen, and A. Voigt, 2013: Robust increase in equilibrium climate sensitivity under global warming. *Geophys. Res. Lett.*, **40**, 5944–5948, https://doi.org/10.1002/2013GL058118.

Pierrehumbert, R. T., 2013: Hot climates, high sensitivity. *Proc. Natl. Acad. Sci. USA*, **110**, 14 118–14 119, https://doi.org/10.1073/pnas.1313417110.

Po-Chedley, S., K. C. Armour, C. M. Bitz, M. D. Zelinka, B. D. Santer, and Q. Fu, 2018: Sources of intermodel spread in the

lapse rate and water vapor feedbacks. *J. Climate*, **31**, 3187–3206, https://doi.org/10.1175/JCLI-D-17-0674.1.

Randall, D. A., and Coauthors, 2018: 100 years of earth system model development. *A Century of Progress in Atmospheric and Related Sciences: Celebrating the American Meteorological Society Centennial*, *Meteor. Monogr.*, No. 59, Amer. Meteor. Soc., https://doi.org/10.1175/AMSMONOGRAPHS-D-18-0018.1.

Rugenstein, M., and Coauthors, 2020: Equilibrium climate sensitivity estimated by equilibrating climate models. *Geophys. Res. Lett.*, **47**, e2019GL083898, https://doi.org/10.1029/2019GL083898.

Sejas, S. A., X. Hu, M. Cai, and H. Fan, 2021: Understanding the differences between TOA and surface energy budget attributions of surface warming. *Front. Earth Sci.*, **9**, 725816, https://doi.org/10.3389/feart.2021.725816.

Senior, C. A., and J. F. B. Mitchell, 2000: The time-dependence of climate sensitivity. *Geophys. Res. Lett.*, **27**, 2685–2688, https://doi.org/10.1029/2000GL011373.

Stolpe, M. B., I. Medhaug, U. Beyerle, and R. Knutti, 2019: Weak dependence of future global mean warming on the background climate state. *Climate Dyn.*, **53**, 5079–5099, https://doi.org/10.1007/s00382-019-04849-3.

Sun, J., M. Secor, M. Cai, and X. Hu, 2024: A quasi-linear relationship between planetary outgoing longwave radiation and surface temperature in a radiative-convective-transportive climate model of a gray atmosphere. *Adv. Atmos. Sci.*, **41**, 8–18, https://doi.org/10.1007/s00376-023-2386-1.

von der Heydt, A. S., and P. Ashwin, 2016: State dependence of climate sensitivity: Attractor constraints and palaeoclimate regimes. *Dyn. Stat. Climate Syst.*, **1**, dzx001, https://doi.org/10.1093/climsys/dzx001.

Yoshimori, M., and M. Suzuki, 2019: The relevance of mid-Holocene Arctic warming to the future. *Climate Past*, **15**, 1375–1394, https://doi.org/10.5194/cp-15-1375-2019.

——, T. Yokohata, and A. Abe-Ouchi, 2009: A comparison of climate feedback strength between CO_2 doubling and LGM experiments. *J. Climate*, **22**, 3374–3395, https://doi.org/10.1175/2009JCLI2801.1.

——, J. C. Hargreaves, J. D. Annan, T. Yokohata, and A. Abe-Ouchi, 2011: Dependency of feedbacks on forcing and climate state in physics parameter ensembles. *J. Climate*, **24**, 6440–6455, https://doi.org/10.1175/2011JCLI3954.1.

Zhang, Y., N. Jeevanjee, and S. Fueglistaler, 2020: Linearity of outgoing longwave radiation: From an atmospheric column to global climate models. *Geophys. Res. Lett.*, **47**, e2020GL089235, https://doi.org/10.1029/2020GL089235.

Zhu, J., and C. J. Poulsen, 2020: On the increase of climate sensitivity and cloud feedback with warming in the community atmosphere models. *Geophys. Res. Lett.*, **47**, e2020GL089143, https://doi.org/10.1029/2020GL089143.

——, ——, and J. E. Tierney, 2019: Simulation of Eocene extreme warmth and high climate sensitivity through cloud feedbacks. *Sci. Adv.*, **5**, eaax1874, https://doi.org/10.1126/sciadv.aax1874.